ACS APPLIED MATERIALS & INTERFACES

Research Article

www.acsami.org

Enhanced Photocatalytic Activity of Ultrathin $Ba_5Nb_4O_{15}$ Two-Dimensional Nanosheets

Sangbaek Park,[†] Hee Jo Song,[†] Chan Woo Lee,[†] Sung Won Hwang,[‡] and In Sun Cho*[,‡]

[†]Department of Materials Science and Engineering, Seoul National University, Seoul 151-744, South Korea

[‡]Department of Materials Science and Engineering, and Department of Energy Systems Research, Ajou University, Suwon 443-749, South Korea

Supporting Information

ABSTRACT: Anisotropic two-dimensional (2D) nanosheets of the layered perovskite, $Ba_5Nb_4O_{15}$, with thicknesses of 5−10 nm and lateral sizes of 300−1200 nm, were synthesized by a hydrothermal route. The influences of the 2D morphology of the material on the crystal and electronic structures, light absorption properties, and photocatalytic activity were investigated. The ultrathin nanosheets showed much-enhanced photocatalytic activity compared to both thick nanosheets (~30 nm) and micrometer-sized particles for the evolution of H_2 from water splitting under UV light illumination. This enhanced activity is predominantly attributed to the larger surface area, higher optical absorption, and charge separation ability of the 2D nanosheet, which results from the variation of the local crystal structure arising from the ultrathin morphology of the $Ba_5Nb_4O_{15}$.

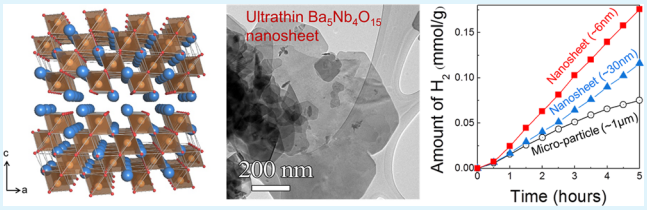

KEYWORDS: *$BaSNb_4O_{15}$, layered perovskite structure, ultrathin nanosheets, hydrothermal, photocatalytic activity, charge separation*

1. INTRODUCTION

Recently, nanomaterials such as nanoparticles, nanorods, nanowires, nanotubes, and nanosheets have been of great interest as novel photocatalysts because they can provide diverse morphological advantages that are beneficial to photocatalytic reactions: large surface areas, relatively short diffusion distances from bulk to surface reactive sites, and enhanced light absorption.[1−7] Nanosheets are one of the most promising candidates, providing high-energy facets, large surface areas, short charge diffusion distances, high charge separation, single-crystalline quality, and diverse chemical composition, all of which lead to high photocatalytic activity.[3,8,9] Cu_2O, $Ca_2Nb_3O_{10}$, WSe_2, and MoS_2 nanosheets have all been demonstrated as excellent photocatalysts for water splitting.[10−13] However, the development of two-dimensional (2D) nanosheets with designed morphologies and chemical components, especially multicomponents, remains a significant challenge because of the lack of effective synthesis methods. Moreover, the influences of the 2D anisotropic morphology on the photophysical and photocatalytic properties of nanosheet materials remain relatively unexplored compared with one-dimensional nanomaterials.

Among various photocatalysts, layered perovskite materials have been found to possess attractive crystal structures for the photocatalytic evolution of H_2 from water splitting. The corner-shared octahedral structure leads to bond angles of metal−oxygen−metal (M−O−M) approaching 180° and the delocalization of excited energy, while the interlayer between perovskite layers can act as a reaction site and also separate oxidation and reduction reaction sites from each other.[14−16] More interestingly, layered perovskite materials are advantageous to form 2D morphologies as a result of the layered nature of the structure.[8,17,18] Layered perovskite structures can be classified into (100), (110), and (111) plane-type structures, depending on the plane of the perovskite layer that is parallel to the interlayer.[16] Various 2D nanosheets with the layered perovskite structure have been reported, including $HCa_2Nb_3O_{10}$,[12] $KCa_2Nb_3O_{10}$,[19] $K_4Nb_6O_{17}$,[20] $Ba_5Ta_4O_{15}$,[17] and $Sr_2Ta_2O_7$.[21] However, reports on nanosheets with the (111) plane-type layered perovskite structure and the photocatalytic H_2 evolution activity of these materials are rare.[17] $Ba_5Nb_4O_{15}$ (BNO) has a hexagonal perovskite crystal structure (space group $P3m1$) with the (111) plane-type structure, which has a high photocatalytic activity for H_2 production from water splitting.[16,22−25] Previous reports have shown that BNO can be synthesized with diverse morphologies by sol−gel, polymerizable complex, or hydrothermal methods, but most of these synthesized materials have large particle sizes or thicknesses.[24−27]

In the present study, ultrathin BNO nanosheets with average thicknesses of ~6 nm were synthesized by a modified hydrothermal method, and the crystal structure, light absorption, electronic structure, morphological features, and photocatalytic activity of the 2D layered perovskite were investigated. The photocatalytic activity was examined by measuring the evolution of H_2 from water splitting under UV-

Received: July 13, 2015
Accepted: September 17, 2015
Published: September 17, 2015

ACS Publications © 2015 American Chemical Society

DOI: 10.1021/acsami.5b06281
ACS Appl. Mater. Interfaces 2015, 7, 21860−21867

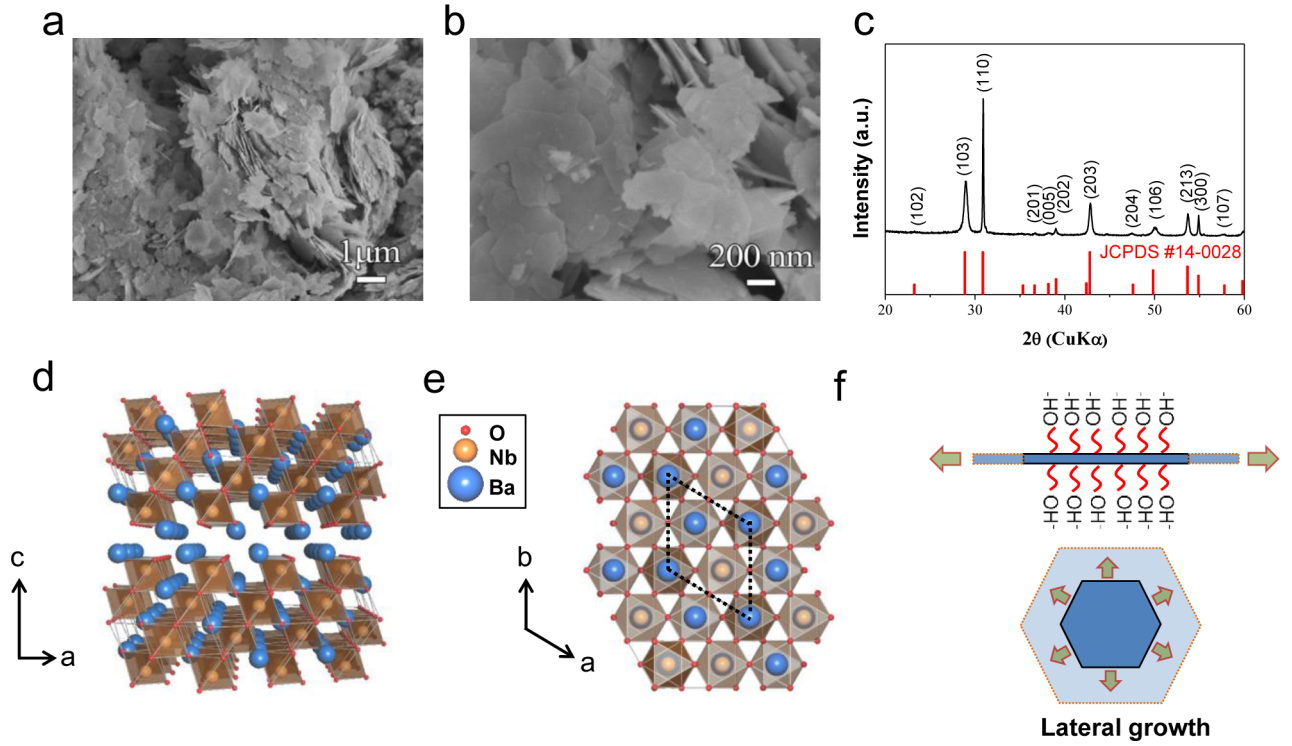

Figure 1. (a, b) SEM images and (c) XRD pattern of the synthesized $Ba_5Nb_4O_{15}$ nanosheets. (d, e) Layered perovskite structure of $Ba_5Nb_4O_{15}$ and (f) growth mechanism of the nanosheet. The OH^- adsorbed onto the (001) planes hinders growth along the [001] direction and thus facilitates growth to form the nanosheet morphology. The arrow indicates growth directions.

light irradiation and compared with that of thick nanosheets (~30 nm) and bulk powders of BNO (~1 μm).

2. EXPERIMENTAL SECTION

Synthesis of BNO Nanosheets. Powders of the BNO nanosheets were prepared by a previously reported hydrothermal route with modifications.[24] Key differences are the use of ethanol/water mixture solvent and niobium chloride ($NbCl_5$) precursor, which is beneficial to synthesize ultrathin BNO nanosheets. All reagents were of analytical grade and used without further purification. In a typical synthesis of the BNO nanosheets, 9.9 mmol of barium nitrate ($Ba(NO_3)_2$, Aldrich Chemicals, 99.0%) and 6.6 mmol of niobium chloride ($NbCl_5$, Aldrich Chemicals, 99.0%) were dissolved in 50 mL of distilled water and 50 mL of absolute ethanol (99.9%), respectively, under constant magnetic stirring. After stirring for 10 min, the $NbCl_5$ solution was slowly added to the $Ba(NO_3)_2$ solution with continued magnetic stirring. The mixed solution was transparent and had a very low pH of <1. The pH of the solution was adjusted very slowly to 13.0 using 1 M NaOH solution. The mixture was then poured into a sealed stainless-steel autoclave with a capacity of 300 mL, heated to 200–250 °C, and held at this temperature for 12 h without stirring. After cooling naturally to room temperature, the product was collected by centrifugation, washed with distilled water and absolute ethanol, and finally dried at 50 °C in an oven. In order to optimize the growth conditions, different growth conditions of temperature (200, 230, and 250 °C), pH (12.0, 12.5, and 13.0), and Ba/Nb ratios (1.5, 1.25 and 1.0) were also investigated. For the purpose of comparison, a bulk BNO powder of micrometer-sized particles was prepared by a solid-state reaction method.[28] Stoichiometric mixtures of $BaCO_3$ (High Purity Chemicals, 99.9%) and Nb_2O_5 (High Purity Chemicals, 99.9%) were homogenized by ball milling with zirconia media for 24 h followed by drying, grinding, and calcination at 1200 °C for 2 h in air.

Characterizations. The crystal structures of the synthesized powders were determined using an X-ray powder diffractometer (XRD; D8-Advance, Bruker Miller Co). The morphologies and microstructures were investigated using a field emission scanning electron microscopy (FESEM; JEOL, JSM-6330F). Transmission electron microscopy (TEM) images and selected area electron diffraction (SAED) patterns were recorded on a JEOL JEM-3000F microscope at an accelerating voltage of 300 kV. The thickness of a nanosheet was measured by atomic force microscopy (AFM, model SPA-400, Seiko, Japan). The UV–visible diffuse reflectance spectra were obtained using a UV–vis spectrophotometer (Hitachi, U-3501). The Raman spectra were recorded using a UV micro Raman spectrometer (Renishaw inVia Reflex). X-ray photoelectron spectroscopy (XPS) spectra were collected using an ESCA spectrometer (Al Kα X-ray source, SIGMA PROBE). The specific surface area measurements were performed using a Brunauer–Emmett–Teller (BET) surface area analyzer (BELSORP-mini II, BEL Japan, Inc.). In order to calculate the electronic band structures of the BNO nanosheets and micrometer-sized particles, both unit cell parameters and atomic coordinates that are determined by the Rietveld refinement were used. The band structure calculations, based on plane wave density functional theory (DFT), were investigated using the CASTEP package program. The applied convergence criteria were 10^{-6} eV for the total energy change per atom. Geometric optimization was performed using a cutoff energy of 380 eV and 4 × 4 × 2 k-point sampling. Generalized gradient approximation (GGA) using Perdewe–Burkee–Ernzerhof (PBE) functionals and ultrasoft pseudopotentials were calculated, and then basis set corrections were conducted.

Photocatalytic Activity Measurements. The photocatalytic reactions were conducted at room temperature in a closed gas circulation system and an outer-irradiation type quartz reactor (200 mL).[29−32] Notably, the light power of outer-irradiation-type systems is much lower than that of the inner-type systems used in previous work on this subject.[31] A 450 W high-pressure mercury lamp was used as the UV light source. The photocatalyst powder (0.1 g) was dispersed in distilled water (120 mL) by magnetic stirring after 10 min of sonication. The amount of H_2 evolved was determined using a gas chromatograph (Donam, DS6200), which was connected to a gas circulating line. NiO_x cocatalysts were loaded by an impregnation method from an aqueous $Ni(NO_3)_2$ solution.[28,32] For the NiO_x-loaded BNO powders, pretreatment by reduction with a H_2 (5%)/Ar (95%)

DOI: 10.1021/acsami.5b06281
ACS Appl. Mater. Interfaces 2015, 7, 21860–21867

gas mixture at 500 °C for 2 h and oxidation with O_2 gas at 200 °C for 1 h was performed.[28]

3. RESULTS AND DISCUSSION

Synthesis of Ultrathin BNO Nanosheets. Parts a and b of Figure 1 show typical SEM images of the BNO nanosheets prepared by the modified hydrothermal method at 230 °C for 12 h and a pH of 13.0. The synthesized BNO is observed to have nanosheet morphology and a contorted hexagonal shape with lateral sizes ranging from 300 nm to ~1.2 μm. In order to obtain phase-pure and ultrathin nanosheets, synthesis parameters such as Ba/Nb ratio, pH, and growth temperature were also investigated (Figures S1–S3 in Supporting Information); the optimal growth conditions were determined to be a Ba/Nb ratio of 1.5, a pH of 13.0, and a temperature of 230 °C. It should be noted that the concentration of the OH^- ions, i.e., high pH (>12.5), is crucial not only for the phase-pure BNO formation but also for the nanosheet (Figure S2). XRD pattern of the synthesized BNO nanosheets is shown in Figure 1c. The BNO nanosheets show peaks correlating to a single-phase perovskite $Ba_5Nb_4O_{15}$ structure, in good agreement with the standard diffraction pattern for the material (JCPDS 14-0028). In addition, the ($h0l$) reflection peaks are broadened in the pattern from the nanosheets, compared to those in the pattern from the micrometer-sized spherical particles prepared by the solid-state reaction method (Figure S4). The intensity ratio of the (110)/(103) peaks for the nanosheets is much higher than that for the micrometer-sized particles, suggesting that the BNO nanosheets have a preferred growth direction along the {110} plane.[8,17] In general, the 2D growth morphologies of materials are associated with the layered crystal structure of the material.[8,17,18,24,25] In the layered compound, the interaction energy between atoms in the same layer usually exceeds that between atoms in adjacent layers; as a result, the nanosheets grow mostly along the edges of individual layers.[17,18] Figure 1d and Figure 1e depict the crystal structure of BNO with the (111) plane-type layered structure along the c axis of the structure. The anisotropic growth of the 2D BNO nanosheets can be interpreted in terms of the intrinsic layered structure and the high concentration of OH^- ions in solution.[8,17] The layered BNO structure contains four NbO_6 octahedral layers separated from each other by Ba^{2+} ions (Figure 1d). Thus, OH^- ions would be preferentially adsorbed on the (001) plane of the nanosheets, i.e., at the exposed Ba^{2+} ions, during the hydrothermal reaction by the Coulombic forces between the positive and negative ions. This adsorption of OH^- would suppress the crystal growth along the ⟨001⟩ directions, as depicted in Figure 1f. It has been reported that OH^- ions are crucial for crystallization because the growth seed is shielded by the OH^- ions, which hinders thickening and facilitates the lateral growth of the nanosheets.[8,17]

In order to understand the formation process of the BNO nanosheets, reaction-time-controlled experiments were conducted at 230 °C and a pH of 13.0. SEM images of the intermediate products, as well as a schematic of the formation process of the nanosheets, are shown in Figure S5. In the first 1 h of the reaction, amorphous nanoparticles were precipitated; these subsequently self-assembled to form nanosheets by oriented attachment after 3 h of reaction.[33−35] After a prolonged reaction time of 6 h, these nanosheets grew laterally because of the hindering effect by the adsorbed OH^- ions on the (001) planes. Finally, the nanosheets were enlarged by Ostwald ripening (12 h). Similar growth processes in layered-structured materials, such as metal niobates, tantalates, and tungstates, have been reported previously.[33,36]

Characterizations of Ultrathin BNO Nanosheets. *1. Thickness and BET Surface Area.* The crystal structure and thickness of the synthesized BNO nanosheets were further characterized by TEM and AFM, respectively. Figure 2a shows

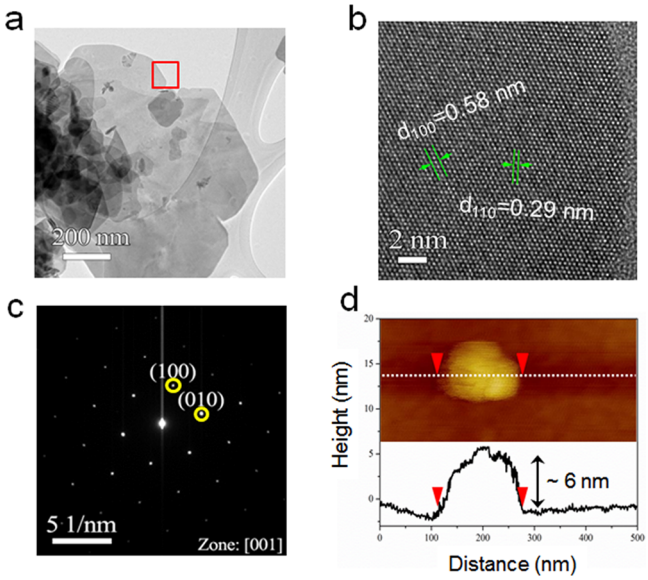

Figure 2. Crystal structure and thickness characteristics: (a) TEM, (b) HR-TEM images, (c) SAED patterns, and (d) AFM image and corresponding height profile of the $Ba_5Nb_4O_{15}$ nanosheet on a Si/SiO_2 substrate.

a TEM image of the ultrathin BNO nanosheets. This confirms the 2D nanosheet morphology of the BNO. A high-resolution TEM image, taken from the region marked in Figure 2a, shows clear lattice fringes even at the edge of the nanosheet, indicating the high crystallinity of the synthesized BNO nanosheets without an amorphous layer. Interplanar spacings of 0.58 and 0.29 nm were observed, which corresponded to the (100) and (110) lattice spacings, respectively, of hexagonal $Ba_5Nb_4O_{15}$. The SAED pattern obtained from an individual nanosheet with a zone axis of [001] shows that the nanosheet is single-crystalline and laterally grown along the [100], [010], and [110] directions (Figure 1c). The thickness of a single layer of the BNO nanosheet was measured by AFM images, revealing that a single layer of the BNO nanosheet has a thickness of ~5.4 ± 1.5 nm (Figure 2d and Figure S6). The surface areas of the ultrathin BNO nanosheets were measured by the BET method. The BNO nanosheets were shown to have a BET surface area of 10.9 m^2/g, 7 times higher than that of the micrometer-sized particles (1.6 m^2/g).

2. Crystal Structure Analysis. The influence of the nanosheet morphology on the crystal structure was investigated by XRD and Raman analysis (Figure 3 and Figure S4). The lattice parameters of the micrometer-sized particles and the nanosheets were calculated from the XRD pattern refinement using the TOPAS software package,[37,38] with results shown in Table 1. As revealed, the nanosheets have smaller c values than the micrometer-sized particles, indicating that the interplanar spacing of the (001) plane in the ultrathin BNO nanosheets is smaller than that of the micrometer-sized particles, corresponding to a reduced unit cell volume. Figure 3a shows the Raman spectra (measured at 25 °C) of the BNO micrometer-sized

DOI: 10.1021/acsami.5b06281
ACS Appl. Mater. Interfaces 2015, 7, 21860−21867

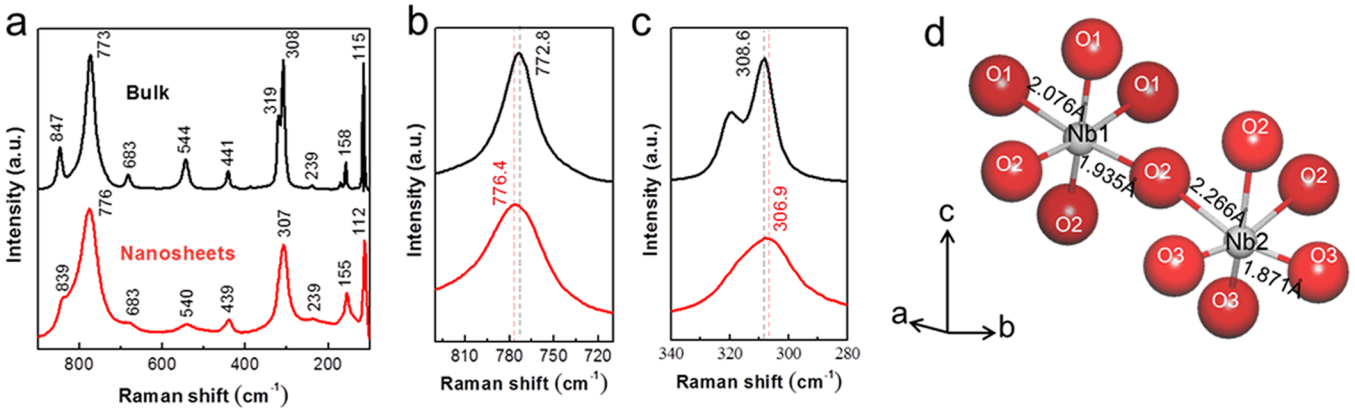

Figure 3. (a) Raman spectra of $Ba_5Nb_4O_{15}$ micrometer-sized particles and nanosheets. Enlarged view of symmetric stretching bands at (b) 780 and (c) 310 cm^{-1}. (d) Bond lengths in NbO_6 octahedra for $Ba_5Nb_4O_{15}$.

Table 1. Calculated Crystal Structure Parameters and BET Surface Areas of the $Ba_5Nb_4O_{15}$ Powders

	lattice parameter, Å					
morphology	*a*	*b*	*c*	γ (deg)	unit cell volume, $Å^3$	surface area, $m^2\ g^{-1}$
micrometer-sized particles	5.800	5.800	11.799	120	343.8	1.6
nanosheets	5.797	5.797	11.754	120	342.1	10.9

particles and nanosheets. The two strongest bands at 308 and 773 cm^{-1} are observed in the spectrum of the micrometer-sized particles, which are associated with symmetric stretching modes in BNO.[39] The correlation between the Raman wavenumbers for stretching and the Nb−O bond lengths in crystalline inorganic niobate compounds has been established; higher wavenumbers of the Raman stretching bands correspond to shorter Nb−O bond lengths.[32,40] Therefore, the Raman peaks at 308 and 773 cm^{-1} are correlated to the longer and shorter Nb−O bond lengths in the NbO_6 octrahedra, respectively. Interestingly, as shown in Figure 3b and Figure 3c, these two stretching peaks for the nanosheets are shifted toward the longer and shorter wavenumber regions, respectively, reflecting slight changes in the Nb−O bond lengths in the nanosheets compared with those in the micrometer-sized particles. As shown in Figure 3d, the nanosheets, compared to the micrometer-sized particles, have slightly shorter Nb1−O1 and Nb2−O2 bond lengths and longer Nb1−O2 and Nb2−O3 bond lengths. The XRD and Raman results both indicate some variation in local crystal structure of the nanosheets, compared with the uniformity of the structure of the micrometer-sized particles.

3. Light Absorption Property and Electronic Band Structure. Figure 4 compares the optical absorption properties of the BNO nanosheets and micrometer-sized particles. The absorption edge of the micrometer-sized particles is estimated to be ~316 nm, which is in good agreement with an earlier report.[28] Meanwhile, the absorption edge of the nanosheets is slightly red-shifted to ~342 nm. In addition, the absorption spectrum of the BNO nanosheets shows a small shoulder at ~380 nm, which may be attributed to defects such as oxygen vacancies.[25−27,41] To obtain a more exact measurement of the band gaps of the BNO nanosheets and micrometer-sized particles, the transition type was characterized from the electronic band structure calculations (discussed later and shown in Figure 5), which revealed that both structures possessed direct band gaps. The optical band gaps were estimated using the following equation:

$$\alpha h\nu = A(h\nu - E_g)^m$$

where α, ν, E_g, and m are the absorption coefficient, frequency, band gap, and characteristic value of the transition (m = 0.5 for a direct band gap), respectively. As shown in Figure 4b, the

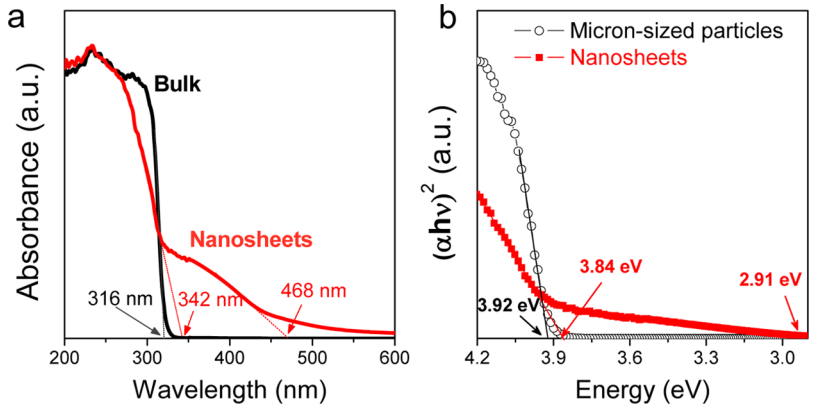

Figure 4. Comparison of light absorption properties of $Ba_5Nb_4O_{15}$ micrometer-sized particles and nanosheets: (a) UV−vis diffuse reflectance spectra and (b) corresponding Kubelka−Munk plot.

DOI: 10.1021/acsami.5b06281
ACS Appl. Mater. Interfaces 2015, 7, 21860−21867

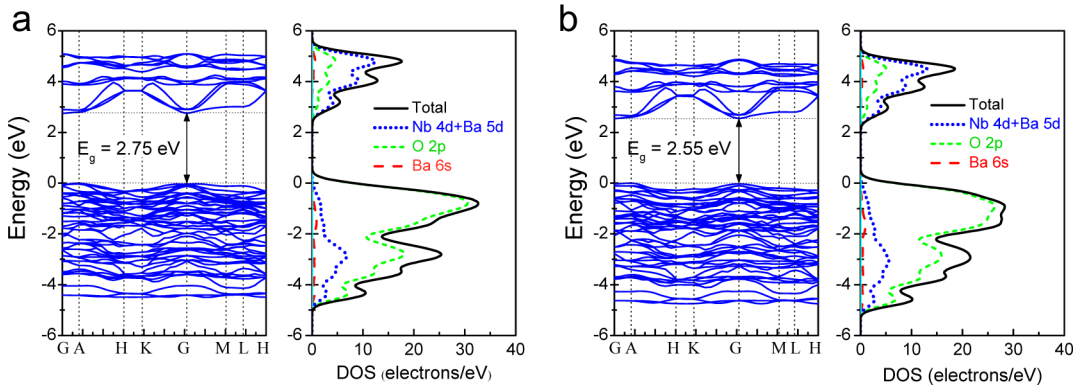

Figure 5. Electronic band structure and density of states (DOS) of (a) micrometer-sized particles and (b) nanosheets.

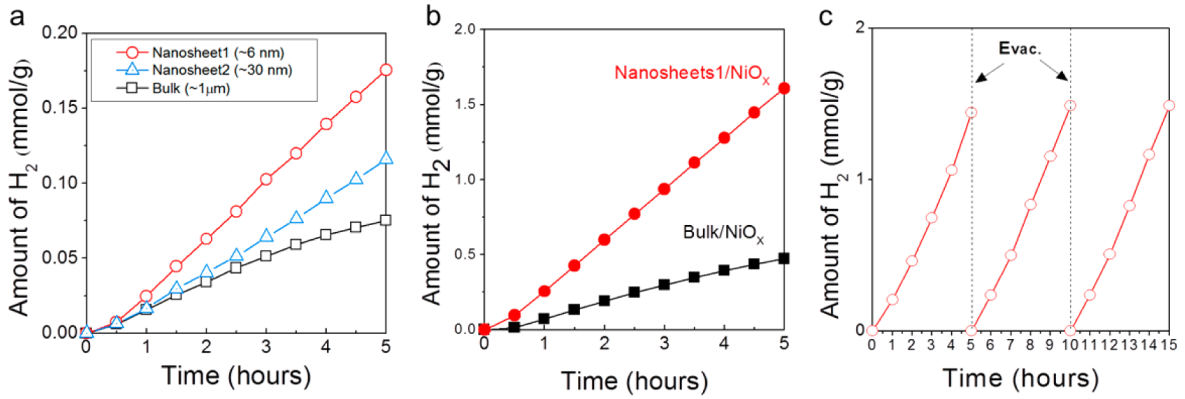

Figure 6. Photocatalytic activity for H_2 evolution using $Ba_5Nb_4O_{15}$ micrometer-sized particles and nanosheets under UV light irradiation: (a) photocatalysts only (nanosheet1, ~6 nm; nanosheet2, ~ 30 nm; micrometer-sized particles), (b) nanosheet1 with NiO_x cocatalyst loading, and (c) stability measurements over 15 h.

estimated band gap of the nanosheets is 3.84 eV, slightly smaller than that of the micrometer-sized particles (3.92 eV). This implies that the nanosheets have an improved light absorption property compared to the micrometer-sized particles. In addition, another sub-band gap of 2.91 eV is observed in the nanosheets, which is considered to arise from the higher amounts of oxygen vacancy defects in the BNO nanosheets (Figure S7).[42,43]

In general, the NbO_6 octahedra in metal niobate compounds affect the band gaps because the O 2p and Nb 4d orbitals mainly contribute to the formation of the valence and conduction bands, respectively. Therefore, changes in the NbO_6 local structure, such as variations in the bond lengths, could induce changes in the band structure and thus affect the optical band gap of the nanosheets. The effect of the local crystal structure variation on the optical absorption properties of the BNO nanosheets was further investigated by calculating the electronic band structure and density of states (DOS) by applying density functional theory (DFT) using the CASTEP program package.[44] The unit cell parameters and atomic coordinates determined by the Rietveld refinement were used for the calculations. Figure 5 shows the electronic band structures and DOS of the BNO nanosheets and micrometer-sized particles. Both nanosheets and micrometer-sized particles have direct band gaps. Additionally, the O 2p and Nb 4d orbitals mostly contribute to the formation of the valence and conduction bands, respectively, which reflects that variations in the local crystal structure, such as Nb−O bond lengths or angles, influence the band gap in BNO, as shown by previous works.[45−49] Therefore, the BNO nanosheets, which have different Nb−O bond lengths, show smaller band gaps (2.55 eV) than the micrometer-sized particles (2.75 eV), which is consistent with the observations in the light absorption measurements (Figure 4). While more intensive studies remain to be performed on the relationship between the Nb−O bond length and the BNO band gap, it can be concluded that the improved light absorption and smaller band gap are related to the local crystal structure variation in the BNO nanosheets, compared with the regularity of the crystal structure of the micrometer-sized particles.

Evaluation of Photocatalytic Activity. Figure 6 shows the photocatalytic activity of the BNO nanosheets and bulk powders for H_2 evolution from water splitting under UV light irradiation. Similar to the previous report,[28] the BNO nanosheets also showed a nearly stoichiometric H_2 and O_2 evolution (H_2/O_2 = 2:1, Figure S8) and the H_2 evolution rate is over 35.2 $\mu mol \cdot h^{-1} \cdot g^{-1}$, which is about 2.3 times higher than that of the micrometer-sized particles (15.0 $\mu mol \cdot h^{-1} \cdot g^{-1}$). This indicates the higher photocatalytic activity of the BNO nanosheets compared to the micrometer-sized particles. However, it should be noted that although the BNO nanosheets show visible light absorption (Figure 4), it does not show any H_2 evolution under visible light irradiation (>420 nm, Figure S9). Moreover, in comparison with ~30 nm thick BNO nanosheets (synthesized at 250 °C, Figure S3), the ultrathin BNO nanosheets (~6 nm) exhibit a photocatalytic activity 1.5 times higher. These results indicate that the morphology and thickness of the BNO largely affect its

DOI: 10.1021/acsami.5b06281
ACS Appl. Mater. Interfaces 2015, 7, 21860−21867

photocatalytic activity. As a cocatalyst, NiO_x was loaded on the surface of the micrometer-sized particles and the nanosheets by impregnation methods[28,32] and the photocatalytic activities of these paired catalysts were also evaluated. As shown in Figure 6b, the photocatalytic activities of both the micrometer-sized particles and the nanosheets increased when the NiO_x cocatalyst is loaded. More interestingly, the photocatalytic activity of the ultrathin BNO nanosheets is greatly increased from 35.2 to 321.6 $\mu mol \cdot h^{-1} \cdot g^{-1}$, which is 3.4 times greater than that of the NiO_x-loaded micrometer-sized particles (94.5 $\mu mol \cdot h^{-1} \cdot g^{-1}$). It is well-known that the photocatalytic activity is mainly determined by the surface area, optical absorption properties, and separation and transport properties of electron−hole pairs.[46−51] The higher surface area increases the number of surface active sites, and the higher light absorption properties (corresponding to the smaller band gap) effectively improve the generation of charge carriers. As shown above, the nanosheets have much larger surface areas and smaller band gaps from the morphological features. Furthermore, the smaller thickness and anisotropic 2D morphology are advantageous for charge separation and transport, which reduces charge recombination and thus facilitates surface charge transfer for water splitting (Figure S10).[52,53] Additionally, the nanosheets have a reduced lattice parameter, and thus a smaller unit cell volume, induced by the variation in the local NbO_6 octahedra along the *c* axis, which broadens the valence band and thus eases the separation of electron−hole pairs along the *c* axis. Furthermore, the BNO nanosheets have exposed facets of (001) planes, compared to the micrometer-sized spherical particles, as shown in TEM analysis (Figure 2), which also contributes the higher photocatalytic activity of the BNO nanosheets by enhancing the charge transfer reaction and adsorption of water molecules on the facets.[54−58] Therefore, all morphological characteristics of the BNO nanosheets, including the larger surface area, improved light absorption, and {001} exposed facets, enhance the photocatalytic activity of the material for H_2 evolution from water splitting. Finally, the stability of the photocatalytic performance was examined by repeating H_2 evolution measurements. As shown in Figure 6c, the BNO nanosheets show stable photocatalytic activity for up to 15 h.

4. CONCLUSIONS

In summary, single-crystalline ultrathin $Ba_5Nb_4O_{15}$ nanosheets with thicknesses of ∼6 nm and lateral sizes of 300−1200 nm were synthesized by a facile hydrothermal method via controlling the reaction temperature, pH, and Ba/Nb ratio. TEM analysis showed that the ultrathin nanosheets had exposed facets of (001) planes and high degrees of crystallinity. The XRD, Raman, and XPS analysis revealed that the nanosheets had variations in local crystal structure and larger amounts of oxygen vacancies compared with the structures of micrometer-sized spherical particles, by which the light absorption properties were improved. In addition, the ultrathin nanosheets showed BET surface areas 7 times larger than the micrometer-sized particles as a result of the 2D anisotropic morphology of the nanosheets. These structural and morphological features of the nanosheets promoted superior photocatalytic activity for H_2 evolution from water splitting under UV light irradiation compared to that of the micrometer-sized particles. The photocatalytic activity was further enhanced by NiO_x cocatalyst loading on the surface; stable H_2 evolution was observed during repeated operations for up to 15 h. Considering the 2D ultrathin nanosheet morphology and high photocatalytic activity of $Ba_5Nb_4O_{15}$, we believe that combining the material with other photocatalysts having smaller band gaps to form type II heterojunctions will enable further improvements in the photocatalytic activity, even permitting H_2 evolution under visible light irradiation.

■ ASSOCIATED CONTENT

Supporting Information

The Supporting Information is available free of charge on the ACS Publications website at DOI: 10.1021/acsami.5b06281.

Effects on crystal structure and morphology, morphological formation process and the corresponding intermediate morphologies, AFM images and height profile, XPS spectra, photocatalytic activity, and fluorescence spectra (PDF)

■ AUTHOR INFORMATION

Corresponding Author

*Phone: +82-31-219-2468. Fax: +82-31-219-1613. E-mail: insuncho@ajou.ac.kr.

Notes

The authors declare no competing financial interest.

■ ACKNOWLEDGMENTS

This work was supported by the new faculty research fund of Ajou University (Grant S-2014-G0001-00309).

■ REFERENCES

(1) Chen, X.; Liu, L.; Yu, P. Y.; Mao, S. S. Increasing Solar Absorption for Photocatalysis with Black Hydrogenated Titanium Dioxide Nanocrystals. *Science* **2011**, *331*, 746−750.

(2) Burda, C.; Chen, X.; Narayanan, R.; El-Sayed, M. A. Chemistry and Properties of Nanocrystals of Different Shapes. *Chem. Rev.* **2005**, *105*, 1025−1102.

(3) Tong, H.; Ouyang, S.; Bi, Y.; Umezawa, N.; Oshikiri, M.; Ye, J. Nano−photocatalytic Materials: Possibilities and Challenges. *Adv. Mater.* **2012**, *24*, 229−251.

(4) Yu, J.; Kudo, A. Effects of Structural Variation on The Photocatalytic Performance of Hydrothermally Synthesized $BiVO_4$. *Adv. Funct. Mater.* **2006**, *16*, 2163−2169.

(5) Kato, H.; Asakura, K.; Kudo, A. Highly Efficient Water Splitting into H_2 and O_2 over Lanthanum-doped $NaTaO_3$ Photocatalysts with High Crystallinity and Surface Nanostructure. *J. Am. Chem. Soc.* **2003**, *125*, 3082−3089.

(6) Chen, D.; Ye, J. $SrSnO_3$ Nanostructures: Synthesis, Characterization, and Photocatalytic Properties. *Chem. Mater.* **2007**, *19*, 4585−4591.

(7) Cho, I. S.; Kim, D. W.; Lee, S.; Kwak, C. H.; Bae, S. T.; Noh, J. H.; Yoon, S. H.; Jung, H. S.; Kim, D. W.; Hong, K. S. Synthesis of Cu_2PO_4OH Hierarchical Superstructures with Photocatalytic Activity in Visible Light. *Adv. Funct. Mater.* **2008**, *18*, 2154−2162.

(8) Wu, J.; Zhang, H.; Du, N.; Ma, X.; Yang, D. General Solution Route for Nanoplates of Hexagonal Oxide or Hydroxide. *J. Phys. Chem. B* **2006**, *110*, 11196−11198.

(9) Bizeto, M. A.; Shiguihara, A. L.; Constantino, V. R. Layered Niobate Nanosheets: Building Blocks for Advanced Materials Assembly. *J. Mater. Chem.* **2009**, *19*, 2512−2525.

(10) Andoshe, D. M.; Jeon, J.-M.; Kim, S. Y.; Jang, H. W. Two-dimensional Transition Metal Dichalcogenide Nanomaterials for Solar Water Splitting. *Electron. Mater. Lett.* **2015**, *11*, 323−335.

(11) Jang, H. S.; Kim, S. J.; Choi, K. S. Construction of Cuprous Oxide Electrodes Composed of 2D Single-crystalline Dendritic Nanosheets. *Small* **2010**, *6*, 2183−90.

DOI: 10.1021/acsami.5b06281
ACS Appl. Mater. Interfaces 2015, 7, 21860−21867

(12) Compton, O. C.; Carroll, E. C.; Kim, J. Y.; Larsen, D. S.; Osterloh, F. E. Calcium Niobate Semiconductor Nanosheets as Catalysts for Photochemical Hydrogen Evolution from Water. *J. Phys. Chem. C* **2007**, *111*, 14589−14592.
(13) Zhao, Y.-F.; Yang, Z.-Y.; Zhang, Y.-X.; Jing, L.; Guo, X.; Ke, Z.; Hu, P.; Wang, G.; Yan, Y.-M.; Sun, K.-N. Cu_2O Decorated with Cocatalyst MoS_2 for Solar Hydrogen Production with Enhanced Efficiency under Visible Light. *J. Phys. Chem. C* **2014**, *118*, 14238−14245.
(14) Kim, J.; Hwang, D. W.; Kim, H. G.; Bae, S. W.; Lee, J. S.; Li, W.; Oh, S. H. Highly Efficient Overall Water Splitting Through Optimization of Preparation and Operation Conditions of Layered Perovskite Photocatalysts. *Top. Catal.* **2005**, *35*, 295−303.
(15) Kudo, A.; Okutomi, H.; Kato, H. Photocatalytic Water Splitting into H_2 and O_2 over $K_2LnTa_5O_{15}$ Powder. *Chem. Lett.* **2000**, *29*, 1212−1213.
(16) Miseki, Y.; Kato, H.; Kudo, A. Water Splitting into H_2 and O_2 over Niobate and Titanate Photocatalysts with (111) Plane-type Layered Perovskite Structure. *Energy Environ. Sci.* **2009**, *2*, 306.
(17) Xu, T. G.; Zhang, C.; Shao, X.; Wu, K.; Zhu, Y. F. Monomolecular-Layer $Ba_5Ta_4O_{15}$ Nanosheets: Synthesis and Investigation of Photocatalytic Properties. *Adv. Funct. Mater.* **2006**, *16*, 1599−1607.
(18) Cho, I.-S.; Kim, D. W.; Cho, C. M.; An, J.-S.; Roh, H.-S.; Hong, K. S. Synthesis, Characterization and Photocatalytic Properties of $CaNb_2O_6$ with Ellipsoid-like Plate Morphology. *Solid State Sci.* **2010**, *12*, 982−988.
(19) Ebina, Y.; Sasaki, T.; Harada, M.; Watanabe, M. Restacked Perovskite Nanosheets and Their Pt-loaded Materials as Photocatalysts. *Chem. Mater.* **2002**, *14*, 4390−4395.
(20) Miyamoto, N.; Nakato, T. Liquid Crystalline Nanosheet Colloids with Controlled Particle Size Obtained by Exfoliating Single Crystal of Layered Niobate $K_4Nb_6O_{17}$. *J. Phys. Chem. B* **2004**, *108*, 6152−6159.
(21) Zhou, C.; Chen, G.; Li, Y.; Zhang, H.; Pei, J. Photocatalytic Activities of $Sr_2Ta_2O_7$ Nanosheets Synthesized by A Hydrothermal Method. *Int. J. Hydrogen Energy* **2009**, *34*, 2113−2120.
(22) Lee, C.-T.; Ou, C.-C.; Lin, Y.-C.; Huang, C.-Y.; Su, C.-Y. Structure and Microwave Dielectric Property Relations in $(Ba_{1-x}Sr_x)_5Nb_4O_{15}$ system. *J. Eur. Ceram. Soc.* **2007**, *27*, 2273−2280.
(23) Ratheesh, R.; Sreemoolanadhan, H.; Sebastian, M. Vibrational Analysis of $Ba_{5-x}Sr_xNb_4O_{15}$ Microwave Dielectric Ceramic Resonators. *J. Solid State Chem.* **1997**, *131*, 2−8.
(24) Wu, S. Y.; Chen, X. M.; Yu, H. Y. Hydrothermal Synthesis of $Ba_5Nb_4O_{15}$ ultrafine powders. *J. Eur. Ceram. Soc.* **2006**, *26*, 1973−1976.
(25) Hsiao, Y.-J.; Chang, Y.-H.; Chang, Y.-S.; Fang, T.-H. Low-Temperature Preparation of $Ba_5Nb_4O_{15}$ Ceramics Through a Sol-Gel Process. *J. Am. Ceram. Soc.* **2007**, *90*, 2287−2290.
(26) Wu, S. Y.; Chen, X. M.; Liu, X. Q. Hydrothermal Derived Barium Niobate Ultra-fine Powders and Nanowires. *J. Alloys Compd.* **2008**, *453*, 463−469.
(27) Zhao, H.; Feng, S.; Xu, W.; Shi, Y.; Mao, Y.; Zhu, X. A Rapid Chemical Route to Niobates: Hydrothermal Synthesis and Transport Properties of Ultrafine $Ba_5Nb_4O_{15}$. *J. Mater. Chem.* **2000**, *10*, 965−968.
(28) Miseki, Y.; Kato, H.; Kudo, A. Water Splitting into H_2 and O_2 over $Ba_5Nb_4O_{15}$ Photocatalysts with Layered Perovskite Structure Prepared by Polymerizable Complex Method. *Chem. Lett.* **2006**, *35*, 1052−1053.
(29) Cho, I. S.; Kim, D. W.; Kim, D. H.; Shin, S. S.; Noh, T. H.; Kim, D. W.; Hong, K. S. Electronic Band Structure, Optical Properties, and Photocatalytic Hydrogen Production of Barium Niobium Phosphate Compounds (BaO-Nb_2O_5-P_2O_5). *Eur. J. Inorg. Chem.* **2011**, *2011*, 2206−2210.
(30) Cho, I. S.; Kwak, C. H.; Kim, D. W.; Lee, S.; Hong, K. S. Photophysical, Photoelectrochemical, and Photocatalytic Properties of Novel $SnWO_4$ Oxide Semiconductors with Narrow Band Gaps. *J. Phys. Chem. C* **2009**, *113*, 10647−10653.
(31) Cho, I.-S.; Bae, S. T.; Kim, D. H.; Hong, K. S. Effects of Crystal and Electronic Structures of ANb_2O_6 (A=Ca, Sr, Ba) Metaniobate Compounds on Their Photocatalytic H_2 Evolution from Pure Water. *Int. J. Hydrogen Energy* **2010**, *35*, 12954−12960.
(32) Cho, I.-S.; Lee, S.; Noh, J. H.; Kim, D. W.; Lee, D. K.; Jung, H. S.; Kim, D.-W.; Hong, K. S. $SrNb_2O_6$ Nanotubes with Enhanced Photocatalytic Activity. *J. Mater. Chem.* **2010**, *20*, 3979.
(33) Chen, X.; Zhou, Y.; Liu, Q.; Li, Z.; Liu, J.; Zou, Z. Ultrathin, Single-crystal WO_3 Nanosheets by Two-dimensional Oriented Attachment Toward Enhanced Photocatalystic Reduction of CO_2 into Hydrocarbon Fuels under Visible Light. *ACS Appl. Mater. Interfaces* **2012**, *4*, 3372−3377.
(34) Schliehe, C.; Juarez, B. H.; Pelletier, M.; Jander, S.; Greshnykh, D.; Nagel, M.; Meyer, A.; Foerster, S.; Kornowski, A.; Klinke, C.; Weller, H. Ultrathin PbS sheets by Two-dimensional Oriented Attachment. *Science* **2010**, *329*, 550−553.
(35) Wang, C.; Du, G.; Ståhl, K.; Huang, H.; Zhong, Y.; Jiang, J. Ultrathin SnO_2 Nanosheets: Oriented Attachment Mechanism, Nonstoichiometric Defects, and Enhanced Lithium-ion Battery Performances. *J. Phys. Chem. C* **2012**, *116*, 4000−4011.
(36) Zhou, L.; Zou, J.; Yu, M.; Lu, P.; Wei, J.; Qian, Y.; Wang, Y.; Yu, C. Green Synthesis of Hexagonal-shaped $WO_3 \cdot 0.33H_2O$ Nanodiscs Composed of Nanosheets. *Cryst. Growth Des.* **2008**, *8*, 3993−3998.
(37) Hoshino, S.; Yamada, K.; Hirao, H. XRD/Rietveld Analysis of The Hydration and Strength Development of Slag and Limestone Blended Cement. *J. Adv. Concr. Technol.* **2006**, *4*, 357−367.
(38) Pourghahramani, P.; Altin, E.; Mallembakam, M. R.; Peukert, W.; Forssberg, E. Microstructural Characterization of Hematite during Wet and Dry Millings Using Rietveld and XRD Line Profile Analyses. *Powder Technol.* **2008**, *186*, 9−21.
(39) Massa, N. E.; Pagola, S.; Carbonio, R. Far-infrared Reflectivity and Raman Spectra of $Ba_5Nb_4O_{15}$. *Phys. Rev. B: Condens. Matter Mater. Phys.* **1996**, *53*, 8148.
(40) Hardcastle, F. D.; Wachs, I. E. Determination of Niobium-oxygen Bond Distances and Bond Orders by Raman Spectroscopy. *Solid State Ionics* **1991**, *45*, 201−213.
(41) George, A.; Virkar, A. Mixed Iono-electronic Conduction in β-$LaNb_3O_9$. *J. Phys. Chem. Solids* **1988**, *49*, 743−751.
(42) Wang, J.; Wang, Z.; Huang, B.; Ma, Y.; Liu, Y.; Qin, X.; Zhang, X.; Dai, Y. Oxygen Vacancy Induced Band-gap Narrowing and Enhanced Visible Light Photocatalytic Activity of ZnO. *ACS Appl. Mater. Interfaces* **2012**, *4*, 4024−4030.
(43) Hsiao, Y. J.; Chang, Y. H.; Chang, Y. S.; Fang, T. H. Low−Temperature Preparation of $Ba_5Nb_4O_{15}$ Ceramics Through a Sol−Gel Process. *J. Am. Ceram. Soc.* **2007**, *90*, 2287−2290.
(44) Clark, S. J.; Segall, M. D.; Pickard, C. J.; Hasnip, P. J.; Probert, M. I.; Refson, K.; Payne, M. C. First Principles Methods Using CASTEP. *Z. Kristallogr.* **2005**, *220*, 567−570.
(45) Maeda, K.; Mallouk, T. E. Comparison of Two- and Three-layer Restacked Dion−Jacobson Phase Niobate Nanosheets as Catalysts for Photochemical Hydrogen Evolution. *J. Mater. Chem.* **2009**, *19*, 4813.
(46) Eng, H. W.; Barnes, P. W.; Auer, B. M.; Woodward, P. M. Investigations of The Electronic Structure of d0 Transition Metal Oxides Belonging to The Perovskite Family. *J. Solid State Chem.* **2003**, *175*, 94−109.
(47) Kato, H.; Kudo, A. Photocatalytic Water Splitting into H_2 and O_2 over Various Tantalate Photocatalysts. *Catal. Today* **2003**, *78*, 561−569.
(48) Wang, J.; Zou, Z.; Ye, J. Surface Modification and Photocatalytic Activity of Distorted Pyrochlore-type Bi_2M(M= In, Ga and Fe)TaO_7 Photocatalysts. *J. Phys. Chem. Solids* **2005**, *66*, 349−355.
(49) Tong, H.; Ouyang, S.; Bi, Y.; Umezawa, N.; Oshikiri, M.; Ye, J. Nano-photocatalytic Materials: Possibilities and Challenges. *Adv. Mater.* **2012**, *24*, 229−51.
(50) Ni, M.; Leung, M. K.; Leung, D. Y.; Sumathy, K. A Review and Recent Developments in Photocatalytic Water-splitting using TiO_2 for Hydrogen Production. *Renewable Sustainable Energy Rev.* **2007**, *11*, 401−425.

DOI: 10.1021/acsami.5b06281
ACS Appl. Mater. Interfaces 2015, 7, 21860−21867

(51) Kudo, A.; Miseki, Y. Heterogeneous Photocatalyst Materials for Water Splitting. *Chem. Soc. Rev.* **2009**, *38*, 253−278.
(52) Li, H.; Liu, C.; Li, K.; Wang, H. Preparation, Characterization and Photocatalytic Properties of Nanoplate Bi_2MoO_6 Catalysts. *J. Mater. Sci.* **2008**, *43*, 7026−7034.
(53) Ida, S.; Ishihara, T. Recent Progress in Two-Dimensional Oxide Photocatalysts for Water Splitting. *J. Phys. Chem. Lett.* **2014**, *5*, 2533−2542.
(54) Li, C.; Han, L.; Liu, R.; Li, H.; Zhang, S.; Zhang, G. Controlled Synthesis of CdS Micro/Nano Leaves with (0001) Facets Exposed: Enhanced Photocatalytic Activity Toward Hydrogen Evolution. *J. Mater. Chem.* **2012**, *22*, 23815−23820.
(55) Liu, G.; Sun, C.; Yang, H. G.; Smith, S. C.; Wang, L.; Lu, G. Q.; Cheng, H.-M. Nanosized Anatase TiO_2 Single Crystals for Enhanced Photocatalytic Activity. *Chem. Commun.* **2010**, *46*, 755−757.
(56) Han, X.; Kuang, Q.; Jin, M.; Xie, Z.; Zheng, L. Synthesis of Titania Nanosheets with A High Percentage of Exposed (001) Facets and Related Photocatalytic Properties. *J. Am. Chem. Soc.* **2009**, *131*, 3152−3153.
(57) Xi, G.; Ye, J. Synthesis of Bismuth Vanadate Nanoplates with Exposed {001} Facets and Enhanced Visible-light Photocatalytic Properties. *Chem. Commun.* **2010**, *46*, 1893−1895.
(58) Bi, Y.; Ouyang, S.; Umezawa, N.; Cao, J.; Ye, J. Facet Effect of Single-crystalline Ag_3PO_4 Sub-microcrystals on Photocatalytic Properties. *J. Am. Chem. Soc.* **2011**, *133*, 6490−6492.

DOI: 10.1021/acsami.5b06281
ACS Appl. Mater. Interfaces 2015, 7, 21860−21867